J|A|C|S ARTICLES

Published on Web 08/24/2009

Tailoring Bicomponent Supramolecular Nanoporous Networks: Phase Segregation, Polymorphism, and Glasses at the Solid−Liquid Interface

Carlos-Andres Palma,[†] Jonas Bjork,[‡] Massimo Bonini,[§] Matthew S. Dyer,[‡] Anna Llanes-Pallas,[⊥] Davide Bonifazi,*[,⊥,¶] Mats Persson,*[,‡] and Paolo Samorì*[,†]

Nanochemistry Laboratory, ISIS - CNRS 7006, Université de Strasbourg, 8 allée Gaspard Monge, 67000 Strasbourg, France, Surface Science Research Centre and Department of Chemistry, University of Liverpool, Liverpool L69 3BX, U.K., BASF SE, GKD/I, 67056 Ludwigshafen, Germany, Dipartimento di Scienze Farmaceutiche, and INSTM UdR di Trieste, Università degli Studi di Trieste, Piazzale Europa 1, 34127 Trieste, Italy, and Department of Chemistry, University of Namur (FUNDP), Rue de Bruxelles 61, 5000 Namur, Belgium

Received April 22, 2009; E-mail: mpersson@liv.ac.uk; davide.bonifazi@fundp.ac.be; samori@isis-ulp.org

Abstract: We study the formation of four supramolecular bicomponent networks based on four linear modules (linkers) bridging melamine via triple hydrogen-bonds. We explore at the nanoscale level the phenomena of polymorphism and phase segregation which rule the generation of highly crystalline nanoporous patterns self-assembled at the solid−liquid interface. The investigated linkers include two systems exposing diuracil groups in the α and ω position, naphthalene tetracarboxylic diimide and pyromellitic diimide. *In situ* scanning tunneling microscopy (STM) investigations revealed that, when blended with melamine, out of the four systems, three are able to form two-dimensional (2D) porous architectures, two of which exhibit highly ordered hexagonal structures, while pyromellitic diimide assembles only into one-dimensional (1D) supramolecular arrays. These bicomponent self-assembled monolayers are used as a test bed to gain detailed insight into phase segregation and polymorphism in 2D supramolecular systems by exploring the contribution of hydrogen-bond energy and periodicity, molecular flexibility, concentration and ratio of the components in solution as well as the effect of annealing via time-dependent and temperature-modulated experiments. These comparative studies, obtained through a joint experimental and computational analysis, offer new insights into strategies toward the bottom-up fabrication of highly ordered tunable nanopatterning at interfaces mediated by hydrogen bonds.

Introduction

By mimicking nature, self-assembly represents the most obvious approach towards molecular engineering, from the molecular to the macroscopic scale.[1−5] The controlled self-assembly of artificial system or biological machinery is based on three milestones: the rational chemical design, the mastering of the system's degrees of freedom and the exploitation of the function intrinsic to the system.[6−10] By reducing the degrees of freedom, 2D self-assembly at interfaces constitutes a model system of study. 2D architectures are of importance for various applications, ranging from nanopatterning[11−16] and rational 3D scaffolding,[17,18] to charge injection at interfaces.[19−25] To this end, during the past decade a rich library of 2D architectures has been self-assembled at interfaces into stable and easily tunable networks featuring a preprogrammed coexistence of long and short-range order.[26−37]

Nowadays, the self-assembly of artificial architectures is widely studied at the solid−liquid and solid-vacuum interfaces.[38−45] The former interface is of special interest because of its analogy to biological processes: upon adsorption at interfaces, (supra) molecules are subjected to complex thermodynamic equilibrium to produce functional architectures. Under these conditions, achieving a full control over complex artificial 2D−3D nanoengineering requires a quantitative description of self-

[†] Université de Strasbourg.
[‡] University of Liverpool.
[§] BASF SE.
[⊥] Università degli Studi di Trieste.
[¶] University of Namur (FUNDP).

(1) Stupp, S. I.; LeBonheur, V.; Walker, K.; Li, L. S.; Huggins, K. E.; Keser, M.; Amstutz, A. *Science* **1997**, *276*, 384–389.
(2) Lehn, J.-M. *Science* **2002**, *295*, 2400–2403.
(3) Whitesides, G. M.; Grzybowski, B. *Science* **2002**, *295*, 2418–2421.
(4) Hoeben, F. J. M.; Jonkheijm, P.; Meijer, E. W.; Schenning, A. P. H. J. *Chem. Rev.* **2005**, *105*, 1491–1546.
(5) Palermo, V.; Samorì, P. *Angew. Chem., Int. Ed.* **2007**, *46*, 4428–4432.
(6) Keser, M.; Stupp, S. I. *Comput. Methods Appl. Mech. Eng.* **2000**, *186*, 373–385.
(7) Rothemund, P. W. K.; Papadakis, N.; Winfree, E. *PLoS Biol.* **2004**, *2*, 2041–2053.
(8) Rothemund, P. W. K. *Nature* **2006**, *440*, 297–302.
(9) Palmer, L. C.; Velichko, Y. S.; Olvera de la Cruz, M.; Stupp, S. I. *Philos. Trans. R. Soc. London, Ser. A* **2007**, *365*, 1417–1433.
(10) de Greef, T. F. A.; Ercolani, G.; Ligthart, G. B. W. L.; Meijer, E. W.; Sijbesma, R. P. *J. Am. Chem. Soc.* **2008**, *130*, 13755–13764.
(11) Theobald, J. A.; Oxtoby, N. S.; Phillips, M. A.; Champness, N. R.; Beton, P. H. *Nature* **2003**, *424*, 1029–1031.
(12) Rosei, F. *J. Phys.: Condens. Matter* **2004**, *16*, S1373–S1436.
(13) Barth, J. V.; Costantini, G.; Kern, K. *Nature* **2005**, *437*, 671–679.
(14) Otero, R.; Rosei, F.; Besenbacher, F. *Annu. Rev. Phys. Chem.* **2006**, *57*, 497–525.

 10.1021/ja9032428 CCC: $40.75

assembly at interfaces taking into account the multiple degrees of freedom of the system under study as well as the experimental conditions. It is well-known that the presence of different structures (i.e., polymorphs) at interface can depend on boundary conditions such as the surface concentration[35,46–50] and the solvent.[27,51–54]

Here we exploit self-recognition of complementary hydrogen-bond moieties based on donor−acceptor−donor (DAD) coupling with acceptor−donor−acceptor (ADA) imidic moieties (Scheme 1). At the vacuum-substrate interface, the pattern formation via self-assembly of these complementary moieties have been shown to depend on temperature, concentration and ratio of the components.[55] In light of this, supramolecular hydrogen-bonded bicomponent 2D networks at solid-solution interfaces represent a suitable workbench for studying the interplay of thermodynamics and kinetics in 2D self-assembly.

Scheme 1. Chemical Structures of the Ditopic Imidic Linkers (**1**−**4**) and Melamine (**MEL**)

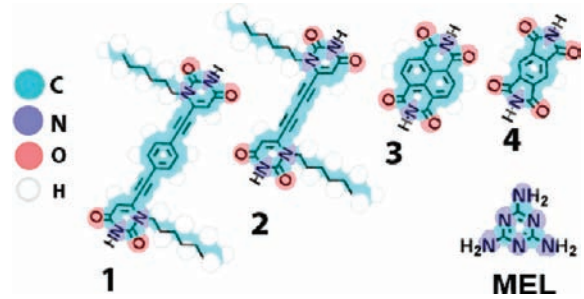

We have addressed our attention to gaining a quantitative understanding on global enthalpy minima which rules the fundamental processes occurring at solid−liquid interfaces such as phase segregation and polymorphism. We have also revealed the key role played by the linker's flexibility in the formation of 2D glasses in self-assembled patterns. These processes are explored by *in situ* scanning tunneling microscopy (STM) at the solid−liquid interface in conjunction with density functional theory (DFT) computations.

Results and Discussion

Generalities of 2D Self-Assembly. Phase segregation and-**polymorphism** are two fundamental phenomena arising during the formation of long-range highly ordered 2D multicomponent networks at the solid−liquid interface. At the solid−liquid interface (nanoscopic) phase segregation can be defined both as the coexistence of multiple segregated phases having different chemical composition adsorbed at the surface (type I)[56] or by the adsorption of only one phase at the interface (type II), leaving the other components in the supernatant solution.[57] For the latter case, under equilibrium conditions, the favored adsorbed phase at the interface is referred to as the thermodynamically stable phase. Such a scenario is favored by tight

(15) Pace, G.; Petitjean, A.; Lalloz-Vogel, M.-N.; Harrowfield, J.; Lehn, J.-M.; Samorì, P. *Angew. Chem., Int. Ed.* **2008**, *47*, 2484–2488.
(16) Madueno, R.; Raisanen, M. T.; Silien, C.; Buck, M. *Nature* **2008**, *454*, 618–621.
(17) El-Kaderi, H. M.; Hunt, J. R.; Mendoza-Cortes, J. L.; Cote, A. P.; Taylor, R. E.; O'Keeffe, M.; Yaghi, O. M. *Science* **2007**, *316*, 268–272.
(18) Ockwig, N. W.; Delgado-Friedrichs, O.; O'Keeffe, M.; Yaghi, O. M. *Acc. Chem. Res.* **2005**, *38*, 176–182.
(19) Love, J. C.; Estroff, L. A.; Kriebel, J. K.; Nuzzo, R. G.; Whitesides, G. M. *Chem. Rev.* **2005**, *105*, 1103–1169.
(20) Vilan, A.; Cahen, D. *Trends Biotechnol.* **2002**, *20*, 22–29.
(21) Choi, B.; Rhee, J.; Lee, H. H. *Appl. Phys. Lett.* **2001**, *79*, 2109–2111.
(22) Hamadani, B. H.; Corley, D. A.; Ciszek, J. W.; Tour, J. M.; Natelson, D. *Nano Lett.* **2006**, *6*, 1303–1306.
(23) Stoliar, P.; Kshirsagar, R.; Massi, M.; Annibale, P.; Albonetti, C.; de Leeuw, D. M.; Biscarini, F. *J. Am. Chem. Soc.* **2007**, *129*, 6477–6484.
(24) Kronemeijer, A. J.; Akkerman, H. B.; Kudernac, T.; van Wees, B. J.; Feringa, B. L.; Blom, P. W. M.; de Boer, B. *Adv. Mater.* **2008**, *20*, 1467.
(25) Müllen, K.; Rabe, J. P. *Acc. Chem. Res.* **2008**, *41*, 511–520.
(26) De Feyter, S.; Miura, A.; Yao, S.; Chen, Z.; Wurthner, F.; Jonkheijm, P.; Schenning, A. P. H. J.; Meijer, E. W.; De Schryver, F. C. *Nano Lett.* **2005**, *5*, 77–81.
(27) Lackinger, M.; Griessl, S.; Heckl, W. M.; Hietschold, M.; Flynn, G. W. *Langmuir* **2005**, *21*, 4984–4988.
(28) Piot, L.; Marchenko, A.; Wu, J.; Müllen, K.; Fichou, D. *J. Am. Chem. Soc.* **2005**, *127*, 16245–16250.
(29) Tahara, K.; Furukawa, S.; Uji-i, H.; Uchino, T.; Ichikawa, T.; Zhang, J.; Mamdouh, W.; Sonoda, M.; De Schryver, F. C.; De Feyter, S.; Tobe, Y. *J. Am. Chem. Soc.* **2006**, *128*, 16613–16625.
(30) Surin, M.; Samorì, P.; Jouaiti, A.; Kyritsakas, N.; Hosseini, M.-W. *Angew. Chem., Int. Ed.* **2007**, *46*, 245–249.
(31) Ma, Z.; Wang, Y.-Y.; Wang, P.; Huang, W.; Li, Y.-B.; Lei, S.-B.; Yang, Y.-L.; Fan, X.-L.; Wang, C. *ACS Nano* **2007**, *1*, 160–167.
(32) Xu, W.; Dong, M.; Gersen, H.; Rauls, E.; Vázquez-Campos, S.; Crego-Calama, M.; Reinhoudt, D. N.; Stensgaard, I.; Laegsgaard, E.; Linderoth, T. R.; Besenbacher, F. *Small* **2007**, *3*, 854–858.
(33) Grill, L.; Dyer, M.; Lafferentz, L.; Persson, M.; Peters, M. V.; Hecht, S. *Nat. Nanotechnol.* **2007**, *2*, 687–691.
(34) Tahara, K.; Lei, S.; Mamdouh, W.; Yamaguchi, Y.; Ichikawa, T.; Uji-i, H.; Sonoda, M.; Hirose, K.; De Schryver, F. C.; De Feyter, S.; Tobe, Y. *J. Am. Chem. Soc.* **2008**, *130*, 6666–6667.
(35) Lei, S.; Surin, M.; Tahara, K.; Adisoejoso, J.; Lazzaroni, R.; Tobe, Y.; Feyter, S. D. *Nano Lett.* **2008**, *8*, 2541–2546.
(36) Mamdouh, W.; Kelly, R. E. A.; Dong, M.; Kantorovich, L. N.; Besenbacher, F. *J. Am. Chem. Soc.* **2008**, *130*, 695–702.
(37) Piot, L.; Palma, C. A.; Llanes-Pallas, A.; Prato, M.; Szekrenyes, Z.; Kamaras, K.; Bonifazi, D.; Samorì, P. *Adv. Funct. Mater.* **2009**, *19*, 1207–1214.
(38) Rabe, J. P.; Buchholz, S. *Science* **1991**, *253*, 424–427.
(39) Cyr, D. M.; Venkataraman, B.; Flynn, G. W. *Chem. Mater.* **1996**, *8*, 1600–1615.
(40) De Feyter, S.; De Schryver, F. C. *Chem. Soc. Rev.* **2003**, *32*, 139–150.
(41) Stohr, M.; Wahl, M.; Galka, C. H.; Riehm, T.; Jung, T. A.; Gade, L. H. *Angew. Chem., Int. Ed.* **2005**, *44*, 7394–7398.
(42) Surin, M.; Samorì, P. *Small* **2007**, *3*, 190–194.
(43) Barth, J. V. *Annu. Rev. Phys. Chem.* **2007**, *58*, 375–375.
(44) Piot, L.; Bonifazi, D.; Samorì, P. *Adv. Funct. Mater.* **2007**, *17*, 3689–3693.
(45) Li, S.-S.; Northrop, B. H.; Yuan, Q.-H.; Wan, L.-J.; Stang, P. J. *Acc. Chem. Res.* **2009**, *42*, 249–259.
(46) Plass, K. E.; Kim, K.; Matzger, A. J. *J. Am. Chem. Soc.* **2004**, *126*, 9042–9053.
(47) Palma, C. A.; Bonini, M.; Llanes-Pallas, A.; Breiner, T.; Prato, M.; Bonifazi, D.; Samorì, P. *Chem. Commun.* **2008**, 5289–5291.
(48) Kampschulte, L.; Werblowsky, T. L.; Kishore, R. S. K.; Schmittel, M.; Heckl, W. M.; Lackinger, M. *J. Am. Chem. Soc.* **2008**, *130*, 8502–8507.
(49) Llanes-Pallas, A.; Palma, C.-A.; Piot, L.; Belbakra, A.; Listorti, A.; Prato, M.; Samorìì, P.; Armaroli, N.; Bonifazi, D. *J. Am. Chem. Soc.* **2009**, *131*, 509–520.
(50) Palma, C.-A.; Bonini, M.; Breiner, T.; Samorì, P. *Adv. Mater.* **2009**, *21*, 1383–1386.
(51) Mamdouh, W.; Uji-i, H.; Ladislaw, J. S.; Dulcey, A. E.; Percec, V.; De Schryver, F. C.; De Feyter, S. *J. Am. Chem. Soc.* **2006**, *128*, 317–325.
(52) Li, Y.; Ma, Z.; Qi, G.; Yang, Y.; Zeng, Q.; Fan, X.; Wang, C.; Huang, W. *J. Phys. Chem. C* **2008**, *112*, 8649–8653.
(53) Florio, G. M.; Ilan, B.; Müller, T.; Baker, T. A.; Rothman, A.; Werblowsky, T. L.; Berne, B. J.; Flynn, G. W. *J. Phys. Chem. C* **2009**, *113*, 3631–3640.
(54) Ilan, B.; Florio, G. M.; Werblowsky, T. L.; Müller, T.; Hybertsen, M. S.; Berne, B. J.; Flynn, G. W. *J. Phys. Chem. C* **2009**, *113*, 3641–3649.
(55) Silly, F.; Shaw, A. Q.; Porfyrakis, K.; Briggs, G. A. D.; Castell, M. R. *Appl. Phys. Lett.* **2007**, *91*, 253109–253113.
(56) In monocomponent systems, phase segregation of type I and polymorphism are identical concepts (see Polymorphism).
(57) Baker, R. T.; Mougous, J. D.; Brackley, A.; Patrick, D. L. *Langmuir* **1999**, *15*, 4884–4891.

molecular packing, where molecule−molecule and substrate−molecule interactions per unit area are maximized. When two or more components are present in the supernatant solution, this can give rise to competitive adsorption phenomena.[31,57–59] Under non-equilibrium conditions, the segregated phase will be composed of the component in the supernatant solution that more quickly crystallizes onto the surface.[60,61] Such a metastable phase is typically promoted by strong molecule−molecule interactions.

Another fundamental aspect at solid−liquid interfaces is the control over polymorphism.[35,46,62,63] Polymorphism is the existence of two or more crystal structures made from the same molecular building-blocks. The structure's short- and long-range crystalline order depends on the number of contained defects. Beyond impurities, these defects can be regarded either as intrinsic[64] or extrinsic (extrinsic defects are mainly due to kinetic traps or substrate commensurability and have also been referred to as "pseudopolymorphs").[46,65] Notably intrinsic defects may lead to the formation of polycrystalline tillings[66] and glasses.[67] A glass can be encompassed inside a broader definition of polymorphism (Greek: *poly* = many, *morph* = form). Here we define a glass as a structure featuring local order through molecular connectivity. For instance the combination of components *A* and *B* can originate a rational sequence (*A*-*B*-*A*-*B*-*A*-) forming a network.[67]

Both polymorphism and segregation concepts are fundamental in bi- and multicomponent self-assembly. To understand their interplay at the solid−liquid interface, the difference in Gibbs free energy between two systems ***a*** and ***b*** (a system consisting of a substrate, a supernatant solution, and physisorbed monolayers) can be ideally described as:

$$\Delta G_{a,b} = G_a - G_b \tag{1}$$

$$G_a = \sum_i \gamma_i[\mathrm{nm}^{-2}] \cdot A_i^{\mathrm{phase}} + \sum_j \mu_j[\mathrm{molecule}^{-1}] \cdot N_j^{\mathrm{solvated}} + \gamma_{\mathrm{substrate/solvent}}[\mathrm{nm}^{-2}] \cdot (A^{\mathrm{total}} - A^{\mathrm{occupied}}) \tag{2}$$

where γ_i is the free energy per unit area of the *i*th phase being part of the system ***a***, A_i^{phase} is the area occupied by the *i*th phase in system ***a***, μ_j is the free energy per molecule in solution of the *j*th component, N_j^{solvated} is the number of molecules in solution of the *j*th component, $\gamma_{\mathrm{substrate/solvent}}$ is the free surface energy, and $A^{\mathrm{occupied}} = \sum_i A_i^{\mathrm{phase}}$ is the total area occupied by the physisorbed monolayers.

When using molecules that are preferentially physisorbed at the interface, two limiting cases can be drawn. In the first case, by employing highly concentrated solutions, the number of molecules in solution is always much higher than that needed to form a tightly packed monolayer. The occupied area is equivalent to the total available area, and the last term in eq 2 tends to zero (since there is no more free surface). The phase's free energy surface term $\gamma_i[\mathrm{nm}^{-2}] \cdot A_i^{\mathrm{phase}}$ is then minimized through the maximization of the number of molecules and interactions per unit area, i.e. tightly packed phases will be favored. It is worth noting that at saturated concentrations the solution free energy term $\sum_j \mu_j[\mathrm{molecule}^{-1}] \cdot N_j^{\mathrm{solvated}}$ still plays a dominant role.[48]

In the second case, by using extremely low analyte concentrations (i.e., sub-monolayer concentrations, having a number of molecules in solution that is lower than that needed to form a tightly packed monolayer[35,50]), the number of molecules in solution N_j^{solvated} is negligible, and the first term $\gamma_i[\mathrm{nm}^{-2}] \cdot A_i^{\mathrm{phase}}$ is dominant. Since the number of molecules is the limiting variable, the area occupied by one phase A_i^{phase} must be expressed as an explicit function of the number of molecules per unit cell in the *i*th phase, and the total number of adsorbed molecules in the *i*th phase becomes:

$$A_i^{\mathrm{phase}} = \frac{A_i^{\mathrm{unit\ cell}}}{\sum_j N_{i,j}^{\mathrm{unit\ cell}}} \cdot \left(\sum_j N_{i,j}^{\mathrm{adsorbed}} \right) \tag{3}$$

where $A_i^{\mathrm{unit\ cell}}$ is the unit cell area of the *i*th phase, $N_{i,j}^{\mathrm{unit\ cell}}$ is the number of molecules of the *j*th component in the unit cell of the *i*th phase and $N_{i,j}^{\mathrm{adsorbed}}$ is the total number of molecules adsorbed in the *i*th phase. Then the first term of eq 2 becomes independent of the unit cell area and will be minimized through the maximization of the number of interactions per molecule in the unit cell.

In the following sections we will describe how both phase segregation and polymorphism can be attributed to the intrinsic chemical design of the molecular building blocks by taking into account the enthalpic contributions to the free energies in eq 2 through their intermolecular energies.

Imaging and Self-Assembly of 2D Networks. Self-assembly of the linkers with melamine into ordered bicomponent networks is successfully obtained by applying 6 ± 1 μL[68] of the proper solutions in a solvent mixture of 1,2,4-trichlorobenzene/dimethylsulfoxide to the basal plane of highly oriented pyrolitic graphite (HOPG) surface. For the four investigated systems (**1**+**MEL**, **2**+**MEL**, **3**+**MEL**, and **4**+**MEL**) an accurate control of the concentration and stoichiometry is needed to favor the formation of a particular bicomponent pattern (see Phase Segregation section). The self-assembly at the solid−liquid interface of the monocomponent systems (linkers **1**, **2**, **3** and **4** and **MEL**) was also studied, and the results are shown in the Supporting Information (Figures S1−S4).

STM images of the bicomponent pattern structure formed by **1**+**MEL**, which has been recently introduced,[47] are further analyzed in Figure 1. The STM constant current images (Figure 1) show various polygonal patterns, characterized by different contrasts. In Figure 1a **MEL** molecules appear brighter when the substrate is biased negative with respect to the tip. This is in accordance with the orbital density plot calculated by DFT

(58) Bonini, M.; Zalewski, L.; Breiner, T.; Dötz, F.; Kastler, M.; Schädler, V.; Surin, M.; Lazzaroni, R.; Samorì, P. *Small* **2009**, *5*, 1521–1526.
(59) Kim, K.; Plass, K. E.; Matzger, A. J. *J. Am. Chem. Soc.* **2005**, *127*, 4879–4887.
(60) Chung, S.-Y.; Kim, Y.-M.; Kim, J.-G.; Kim, Y.-J. *Nat. Phys.* **2008**, *5*, 68–73.
(61) Ostwald, W. Z. *Z. Phys. Chem* **1897**, *22*, 289–330.
(62) Bernstein, J. *Polymorphism in Molecular Crystals*; Oxford University Press: New York, 2002.
(63) Desiraju, G. R. *Cryst. Growth Des.* **2008**, *8*, 3–5.
(64) Here forth, we consider a property to be "intrinsic" (or intensive) when it belongs mostly to the design of a single molecular building block, and "extrinsic" (or extensive) when it belongs to an ensemble.
(65) Bernstein, J. *Cryst. Growth Des.* **2005**, *5*, 1661–1662.
(66) Blunt, M. O.; Russell, J. C.; Gimenez-Lopez, M. d. C.; Garrahan, J. P.; Lin, X.; Schroder, M.; Champness, N. R.; Beton, P. H. *Science* **2008**, *322*, 1077–1081.
(67) Otero, R.; Lukas, M.; Kelly, R. E. A.; Xu, W.; Laegsgaard, E.; Stensgaard, I.; Kantorovich, L. N.; Besenbacher, F. *Science* **2008**, *319*, 312–315.

(68) This particular volume is chosen since it is the one needed for TCB to completely wet 1 cm^2 of HOPG, giving a scanning window of ~3 h before dewetting occurs due to evaporation of the solvent.

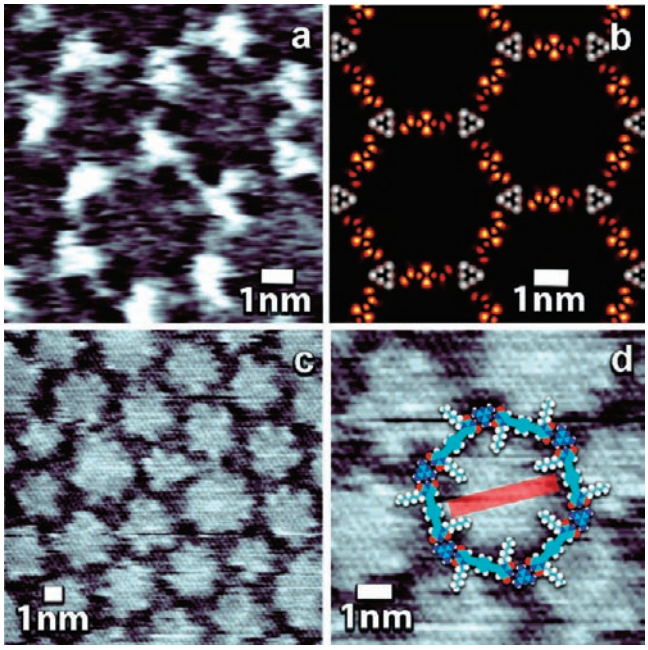

Figure 1. (a), (c), (d) Constant current STM images of**1**+**MEL**. (a) Zoom-in of a small crystalline domain showing a pentagon defect. (b) Simulated STM images at constant height: in white at (E_F − 0.72) eV and in red at (E_F + 0.83) eV. (c) Survey STM image showing a polygonal motif. (d) Zoom-in with superimposed molecular models; the red bar corresponds to 3.2 nm. Tunneling parameters: (a) average tunneling current I_t = 0.5 pA, sample bias voltage V_t = −500 mV; (c), (d) I_t = 5 pA, V_t = −500 mV.

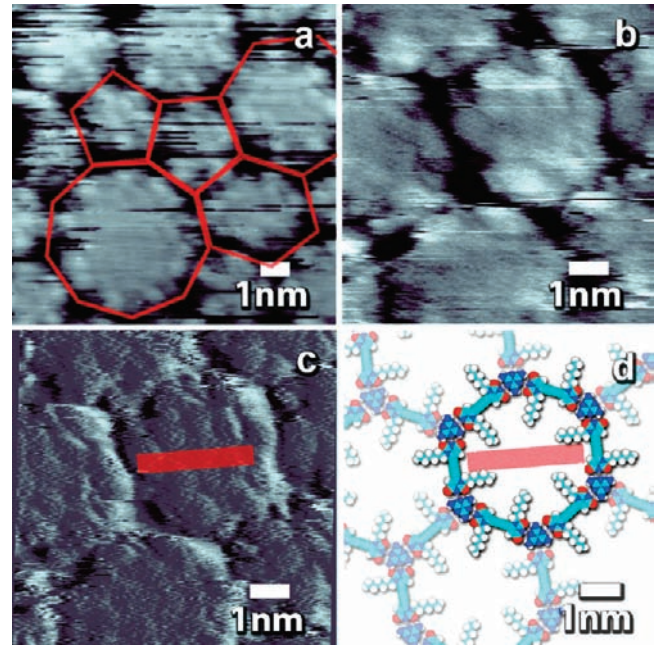

Figure 2. STM images of**2**+**MEL** recorded in (a), (b) constant current mode and (c) constant height. (d) Molecular model of a hexagonal structure (red bars correspond to 2.8 nm). (a) A nonagon surrounded by pentagons and a hexagon is shown. Tunneling parameters: (a) I_t = 4 pA, V_t = −900 mV; (b) I_t = 5 pA, V_t = −900 mV; (c), (d) I_t = 5 pA, V_t = −900 mV.

corresponding to a constant height STM image through the Tersoff−Hamann approximation,[69,70] shown in Figure 1b. The latter exhibits two optimized hexagons, in which **MEL** (white) corresponds to the orbital densities from four degenerated states at −0.72 eV below the Fermi energy of graphite. Linker **1** (red) corresponds to the orbital densities from three degenerated states at 0.83 eV above the Fermi energy of graphite. The HOMO of **MEL** is closer to the substrate's Fermi level than the HOMO of **1** (see Supporting Information, Figure S5). This is in line with the higher current contrast of **MEL** when imaged at negative bias voltages. Despite the theoretical prediction of a higher contrast of the **MEL** molecules at negative biases, in most cases (∼80%) a brighter contrast appears inside the pore areas in the constant current images, under both positive and negative biases (Figure 1c and d). This bright contrast remains elusive and may mostly be ascribed to solvent molecules coadsorbed at surfaces.[71] This leads to an inversion of the contrast: **MEL** molecules thus appear as wide black spots (c and d of Figure 1).

Similarly, the **2**+**MEL** system on HOPG exhibits self-assembled patterns featuring polygonal structures (Figure 2a). This pattern is characterized by a much higher polygon distribution; it is possible to identify a nonagon (red wire frames) evidenced by nine darker spots acting as corners. As previously discussed, most dark spots correspond to the location of the **MEL** molecules, as also revealed by comparing panels b−d of Figure 2. Again, a brighter contrast is observed in the pores for the case of the constant current images (Figure 2a,b). The predicted hexagonal motif with molecular models is shown in Figure 2d (the red bar corresponds to 2.8 nm). The absence of spatially extended single crystalline domains did not allow us to determine the unit cell for the predicted hexagonal self-assembled network. For sake of simplicity, this so-formed glass phase can be better understood when classified in terms of a collection of local polymorph structures (*vide infra* Polymorphism section).

While in the networks obtained with the two previous linkers polymorphism is expressed through the formation of different polygons, in mixtures of **3**+**MEL** polymorphism arises from the coexistence of one-dimensional supramolecular linear assemblies (Figure 3a,b - gray arrow) and porous hexagonal networks (Figure 3a,b - black arrow) formed by alternating units of **MEL** and **3**. With increasing concentration of **MEL** in solution (up to 40 μM in **MEL** added to 6 μM **3**+**MEL** solutions, *vide infra* in Phase Segregation section), only the highly ordered hexagonal pattern is formed (Figure 3c,d), remarkably correlating with the superimposed molecular models (Supporting Information, Figure S9 shows a zoom-in of the superimposed models in which the superimposed molecular error is less than 1%). Again, in the constant current images (Figure 3d), a higher contrast is seen on the inside of the pores. This pore contrast is much brighter and regular than that observed for the assemblies **1**+**MEL** and **2**+**MEL**, which we attribute to the coadsorption of **MEL** in the hexagon's pores. (Supporting Information, Figures S9 and S12, and Polymorphism section).

Conversely, a markedly different self-assembly behavior has been observed for the **4**+**MEL** mixture revealing the formation of linear supramolecular polymers (Figure 4).[72] The linear arrangement obtained with the **4**+**MEL** system differs in its structural parameters from that of **3**+**MEL**. Narrow *inter-row* distances allow extra H-bonding interaction of linker **4**+**MEL**

(69) Tersoff, J.; Hamann, D. R. *Phys. Rev. Lett.* **1983**, *50*, 1998–1998.
(70) Tersoff, J.; Hamann, D. R. *Phys. Rev. B* **1985**, *31*, 805–805.
(71) The contribution of the solvent molecules co-adsorbed on the surface to the contrast has been already reported on porous structures: Gutzler, R.; Lappe, S.; Mahata, K.; Schmittel, M.; Heckl, W. M.; Lackinger, M. *Chem. Commun.* **2009**, 680–682, whereas the spontaneous contrast changes in the pores during scans would support the hypothesis of adsorption of molecules on the tip, changing its work function.

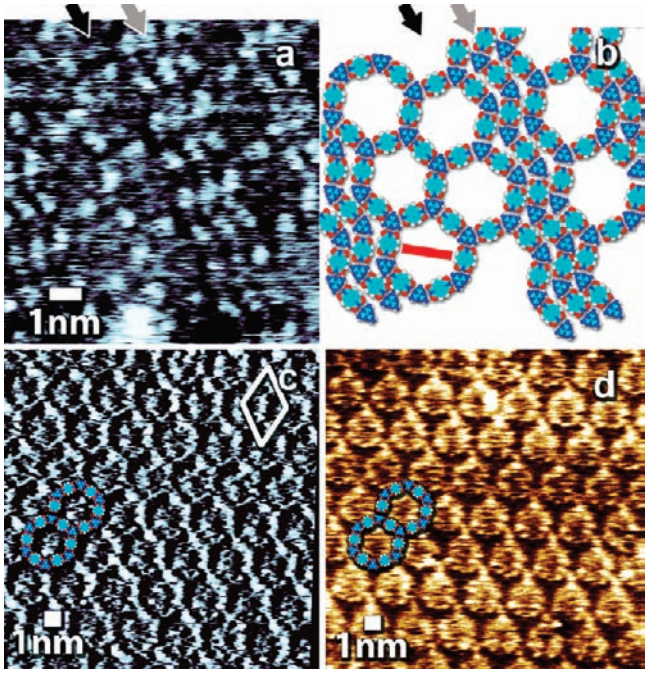

Figure 3. STM images of **3**+**MEL** recorded in (a), (c) constant current, and (d) constant height mode. (a) By applying a 6 μM equimolar solution of **3**+**MEL** a 1D-chain polymorph (gray lines) and the predicted hexagonal motif (black arrows) are obtained. (b) Proposed 2D packing motif. The red bar corresponds to 1.6 nm. (c), (d) The long-range highly ordered pattern formed at higher **MEL** concentrations. Unit cell parameters: $a = 2.8 \pm 0.2$ nm, $b = 2.8 \pm 0.2$ nm, with $\gamma = 58 \pm 3°$. Tunneling parameters: (a) $I_t =$ 10 pA, $V_t = -500$ mV. (c), (d) $I_t = 5$ pA, $V_t = -150$ mV.

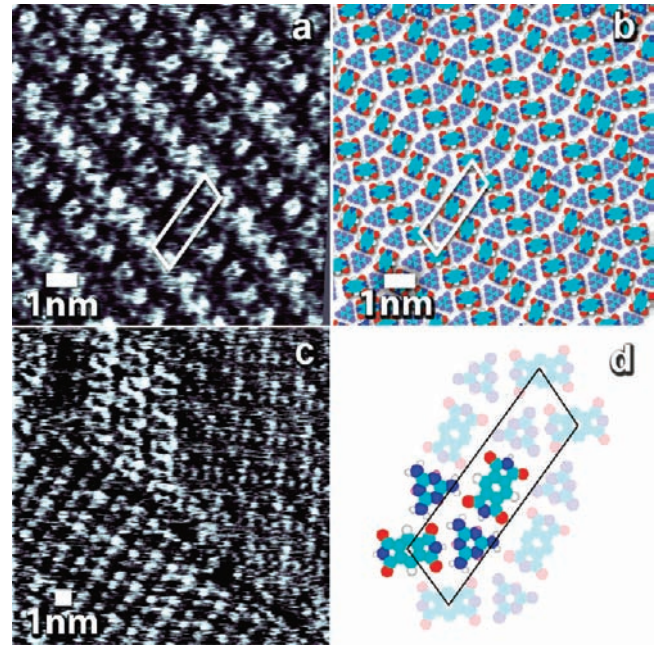

Figure 4. (a,c) Constant current STM images of the dominant polymorph formed by **4**+**MEL**. (a) Unit cell parameters: $a = 2.6 \pm 0.2$ nm, $b = 0.8 \pm 0.1$ nm, $\gamma = 83 \pm 3°$).(b) Proposed molecular arrangement. (c) An image showing different polymorphic domains of **4**+**MEL**. (d) Proposed structure of the molecular assembly. The highlighted [(**4**)$_2$(**MEL**)$_2$] tetramer has been planarized and then minimized using the MM2 force field. Tunneling parameters: (a) $I_t = 15$ pA, $V_t = 300$ mV; (c) $I_t = 20$ pA, $V_t = 500$ mV.

with an additional melamine belonging to the adjacent row (Figure 4d). The tetramer [(**4**)$_2$(**MEL**)$_2$] shown in Figure 4d represents a MM2 force field minimized complex, in which all hydrogen-bond lengths are found to be less than 1.9 Å, being in accordance with typical hydrogen-bond distances.[73] Supporting Information Figure S12 depicts a DFT minimized [(**4**)$_2$(**MEL**)$_2$] tetramer, where the hydrogen-bond energy gain between the adjacent melamine and the [(**4**)$_2$(**MEL**)] trimer was found to be 0.215 eV. Interestingly when a similar tetramer was minimized using linker **3**, [(**3**)$_2$(**MEL**)$_2$] no H-bond was formed, and the stabilization energy gain was only 0.015 eV.

Phase Segregation in 2D Networks. Phase segregation at solid−liquid interface is highly dependent on the concentration of the components in the solution and on the type of solvent. In bicomponent systems, the enthalpic driving force for the formation of these phases is mostly arising from the competition between homo- and hetero-recognition through hydrogen bonds. The nature itself of the chosen DAD···ADA complementary sequence implies that homo-recognition can occur, leading to monocomponent aggregation through dihapto hydrogen bonds. As aforementioned, the formation of multiple phases can be described in terms of phase segregation of type I, due to the presence of multiple components having different chemical composition coexisting on the surface, or type II, where competitive adsorption determines the presence of only one phase physisorbed at the interface. Scheme 2 illustrates both types of phase segregation in our systems. We had previously introduced[47] that, in pattern **1**+**MEL**, competitive adsorption can be suppressed completely by employing low concentration solutions, below monolayer concentrations. Figure S6 in the Supporting Information depicts a phase diagram showing that when the concentration is increased, segregated phases of **MEL** and **1** start being observed. These phases coexist with crystal and glass structures of **1**+**MEL** at equimolar concentration ranges from 12 μM up to 50 μM solutions (see Supporting Information, Figure S10). Exclusive phases of **1**+**MEL** have been found at concentrations around 3 μM.

Similarly, bicomponent patterns based of **2**+**MEL** have been imaged using equimolar solution concentrations around 15 μM. At equimolar concentrations of **2** and **MEL** ranging from 50 μM to 60 μM, only domains of pure **MEL** were found. Note that this phase segregation can be described as type II, since molecule **2** was never observed to (co) physisorb at surfaces when equimolar solutions of **2**+**MEL** were employed. At even lower concentrations, i.e. 3 μM equimolar, no physisorbed pattern was found at the solid−liquid interface by STM imaging.

Remarkably, in contrast to the previous systems, at low concentrations of **3**+**MEL** a tightly packed bicomponent pattern has been observed (Figure 3a, gray lines). At equimolar concentrations of 6 ± 2 μM of **MEL** and **3**, linear 1D supramolecular assemblies (see Figure 3b) are mostly formed. The porous hexagons shown in a and b of Figure 3 are stochastically observed at phase boundaries. When an excess of **MEL** (5 μL of 43 μM solutions) is added to low-concentrated solutions of **3** (6 μL of 6 μM solutions), the linear 1D assembly quickly disappears whereas highly

(72) It is worth noting that it was not possible to visualize the monocomponent monolayers of **4** when deposited using a wide range of solution concentrations, even up to 60 μM. Saturated solutions of **4** could not be imaged by STM because of excessive (non-)faradaic currents.

(73) Jeffrey, G. A. *An Introduction to Hydrogen Bonding*; Oxford University Press: New York, 1997.

Table 1. Potential Energy Contributions (As Absolute Values) from Hydrogen Bond Energies ($E_{H\text{-}bond}$), per Unit Area and per Molecule, from Equations 5 (Column 5) and 4 (Column 6), Respectively[a]

i phase	$A^{unit\ cell}$ [nm^{-2}] exp.	$A^{unit\ cell}$ [nm^{-2}] theory	interactions (M) and molecules (N) in unit cell M_n	N_j	$E_{H\text{-}bond}$[b] [eV] triple	$E_{H\text{-}bond}$[b] [eV] double	potential energy per area $(M \cdot E_{H-bond})/(A^{unit\ cell}) \cdot A^{phase}$ [eV]	potential energy per molecule $(M \cdot E_{H\text{-}bond})/(N^{unit\ cell}) \cdot N^{adsorbed}$ [eV]
MEL[c] polymorph a	0.9 ± 0.1	−	3 triple	2	−	0.437	1.457	0.655
MEL[c] polymorph b	0.8 ± 1	−	3 triple	2	−	0.437	1.639	0.655
1	1.4 ± 0.2	−	1 double	1	−	0.525	0.375	0.525
1+**MEL** hexagonal	13.4 ± 0.6	15.3	3 triple	2 (**MEL**) 3 (**1**)	0.778	−	0.306	0.934
2	−	−	−	−	−	0.507	−	−
2+**MEL** hexagons	12.4 ± 1.4	10.9	6 triple	2 (**MEL**) 3 (**2**)	0.772	−	0.427	0.926
3	1.6 ± 0.6	−	1 double	1	−	0.488	0.294	0.488
3+**MEL**hexagonal	6.4 ± 0.3	6.2	6 triple	2 (**MEL**) 3 (**3**)	0.718	−	0.693	0.862
3 **MEL** hexagon + coadsorbed MEL	6.4 ± 0.3	6.2	6 triple 3 double	5 (**MEL**) 3 (**3**)	0.718	0.228	0.803	1.000 (for 2 **MEL** in a unitcell)
3+**MEL** chains	1.97 ± 0.5	−	4 triple	2 (**MEL**) 2 (**3**)	0.718	0.015[d]	1.451	0.725
4	−	−	−	−	−	0.525	−	−
4+**MEL** hexagonal	−	5.8	6 triple	2 (**MEL**) 3 (**4**)	0.721	−	0.745	0.866
4+**MEL** chains	1.95 ± 0.5	−	4 triple 2 double	2 (**MEL**) 2 (**4**)	0.721	0.215	1.699	0.829

[a] The theoretical and experimental unit cell areas $A^{unit\ cell}$ are given, and the theoretical values are used for calculation, when available; "−" indicates unavailable or not applicable data. Note that for ease of comparison between *potential energy per unit area* and *per molecule*, the columns are multiplied respectively by the total area in a phase, A^{phase} which is set to 1 nm^{-2}, and the total adsorbed number of molecules $N^{adsorbed}$ which is set to 1 (i.e. like one single component despite dealing with bicomponents). [b] Except for the hexagonal porous networks in Table 2, all other $E_{H\text{-}bond}$ energies are approximated as the energy of interaction of single isolated dimers and not of periodic monolayers. [c] A full description of these two polymorphs can be found in refs 76 and 77. [d] Weak stabilization energy found for the secondary interow **MEL** interaction in a [(**3**)$_2$(**MEL**)$_2$] tetramer, see Supporting Information, Figure S12.

ordered hexagonal networks appear (c and d of Figure 3). Finally, at high equimolar concentrations (25 and 50 μM) of **MEL** and **3** there is a coexistence of several domains featuring the same hexagonal structures of those depicted in c and d of Figure 3, as indicated in Supporting Information, Figure S8. As previously argued, this is most probably due to simultaneous coadsorption of **MEL** with linker **3** and is discussed in the Polymorphism section below.

The coexistence of multiple patterns was often observed for the **4**+**MEL** system, a behavior that seemed to be independent of the concentration. At least three different patterns were imaged when using equimolar solution concentrations from 7 to 43 μM, with the dominant pattern being the one shown in Figure 4a. Figure 4c displays a pattern typical of high concentration solutions of system **4**+**MEL**, with the bottom left corner corresponding to the linear supramolecular chains already shown in Figure 4a,b. Because of the additional ability of **4** to form other complexes such as [(**4**)$_2$(**MEL**)$_2$] tetramer, alternative configurations can be observed on the surface, thus the packing is difficult to predict.

As previously introduced, phase segregation and phase transformations can be quantitatively analyzed through the energetic contributions of the respective phases. To a first approximation, in our case the dominant contribution to the enthalpy of the adsorbed phase is given by the hydrogen-bond interaction. Although van der Waals[74] and dipole−dipole[75] interactions play also an important role, they are usually one order of magnitude lower per molecule than hydrogen bonds. Under this assumption, the left-hand-side term in eq 2 can be approximated as the *potential energy per unit area* arising from hydrogen-bond interactions, multiplied by the area occupied by the phase A_i^{phase}, and calculated as:

$$\gamma_i[\mathrm{nm}^{-2}] \cdot A_i^{phase} \sim \frac{\sum_n M_{i,n}^{unit\ cell} \cdot E_{H\text{-}bond}}{A_i^{unit\ cell}} \cdot A_i^{phase} \qquad (4)$$

where we take into account n types of H-bond interaction energies $\boldsymbol{E}_{\mathbf{H\text{-}bond}}$ and $M_{i,n}^{unit\ cell}$ interactions in a unit cell area $A_i^{unit\ cell}$. The term $\boldsymbol{E}_{\mathbf{H\text{-}bond}}$ is defined as the gain in energy of formation between the isolated molecules and the 2D architecture of interest. First, the difference between the energies of isolated molecules of interest in their relaxed state and those in the minimized 2D architecture (dimers, trimers, repeated monolayer, etc.) is taken, and $\boldsymbol{E}_{\mathbf{H\text{-}bond}}$ is then given by this difference divided by the number of consecutive triple or double H-bonds formed. $\boldsymbol{E}_{\mathbf{H\text{-}bond}}$ energies were calculated through DFT using the PW91 functional and a plane wave basis set (see Experimental Section). Our level of theory gives similar results for the **MEL-MEL D$_3$**-dimer; in other words, formation energies being 0.437 eV (this work), 0.48 eV and 0.44 eV by using the PBE functional.[76,77] For the system of linker **1**, patterns of **1** and patterns of **MEL** are predicted to be the dominant ones over the porous structure since they have the highest (in absolute values) *potential energy per unit area* − provided that enough molecules are present to satisfy the packing density through the whole area (Table 1). For the system of linker **2**, **MEL** is also by far the most favored phase. For linker **3**, the close packed polymorphs of **3**+**MEL** is predicted, having a similar *potential energy per unit area* to packed structures of **MEL**. The linear assembly of **4**+**MEL** is also predicted. Except for the close packed pattern of **3**+**MEL** which will be addressed further on, the

(74) Weber, U. K.; Burlakov, V. M.; Perdigao, L. M. A.; Fawcett, R. H. J.; Beton, P. H.; Champness, N. R.; Jefferson, J. H.; Briggs, G. A. D.; Pettifor, D. G. *Phys. Rev. Lett.* **2008**, *100*, 156101–156104.
(75) Ciesielski, A.; Piot, L.; Samorì, P.; Jouaiti, A.; Hosseini, M. W. *Adv. Mater.* **2009**, *21*, 1131–1136.
(76) Mura, M.; Martsinovich, N.; Kantorovich, L. *Nanotechnology* **2008**, *19*, 465704–465704.
(77) Silly, F.; Shaw, A. Q.; Castell, M. R.; Briggs, G. A. D.; Mura, M.; Martsinovich, N.; Kantorovich, L. *J. Phys. Chem. C* **2008**, *112*, 11476–11480.

Scheme 2. Phase Segregation in Bicomponent Networks[a]

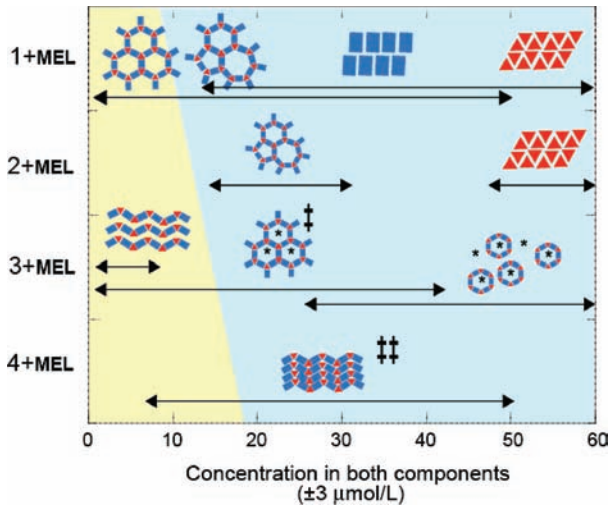

[a] Illustrations show crystals, glasses or disordered structures formed by melamine (red triangles) and the linker (blue rectangles) spanning over the concentrations indicated by their corresponding black arrows. Regions where the black arrows overlap depict phase segregation of type I, while regions where the arrows do not overlap are subject to competitive adsorption, i.e. type II phase segregation. (*) Indicates unresolved (pore) areas by STM. (‡) Only when the concentration of the linker is low (see text). (‡‡) Other unresolved segregated polymorphs where observed. The yellow region corresponds to the concentration needed to fully form a porous monolayer over 1 cm^2 of substrate by applying 5 μL of solution, and as such coincides with the region where the highest *potential energy per molecule* is predicting the most stable pattern (Table 1).

most stable phases predicted are in agreement the observations at (equimolar) solution concentrations higher than a monolayer of the respective lowest-density phase (blue region, Scheme 2). It is interesting to note that the phase segregation of component **3** is not predicted theoretically, being in agreement with our observations, since at (equimolar) high concentrations the *potential energies per area* of the mixed tightly packed components of **3**+**MEL** (1.451 eV) are much greater than the single components of **3** (0.294 eV). Although neither theoretical nor experimental data were available for component **4**, a behavior similar to that of **3** is expected, which explains why there is no phase separation of the linker molecules for all the phases other than that of **1** (since **1** cannot form chain-like structures with **MEL**).

When not enough molecules are present at the interface for forming a full monolayer of the lowest-density phase (yellow zone, Scheme 2), the system's free energy in eq 2 is minimized for those unit cells where the (absolute) *potential energies per molecule* arising from hydrogen-bond interactions are maximum; using eqs 3 and 4:

$$\gamma_i[\mathrm{nm}^{-2}] \cdot A_i^{\mathrm{phase}} \sim \frac{\sum_n M_{i,n}^{\text{unit cell}} \cdot E_{\text{H-bond}}}{\sum_j N_{i,j}^{\text{unit cell}}} \cdot \left(\sum_j N_{i,j}^{\text{adsorbed}} \right) \tag{5}$$

where multiplication by the total number of adsorbed *j*th components ($\sum_j N_{i,j}^{\text{adsorbed}}$), gives the total potential energy in an *i*th phase. Again, the calculated *potential energies per molecule* agree very well with our qualitative STM observations, predicting the segregation and formation of a porous network of **1**+**MEL** and **2**+**MEL** at low concentrations. The formation of the tightly packed and porous structures of **3**+**MEL** constitutes a fascinating case of polymorphism and is described further on. In Table 1 the difference between theoretical porous phases and tightly packed structures of **4**+**MEL** reduces to a few (~37) meV. Since van der Waals interactions are expected to be higher for the tightly packed structure, Scheme 2 is also consistent with the predicted formation of tightly packed polymorphs of **4**+**MEL** through the whole concentration range.

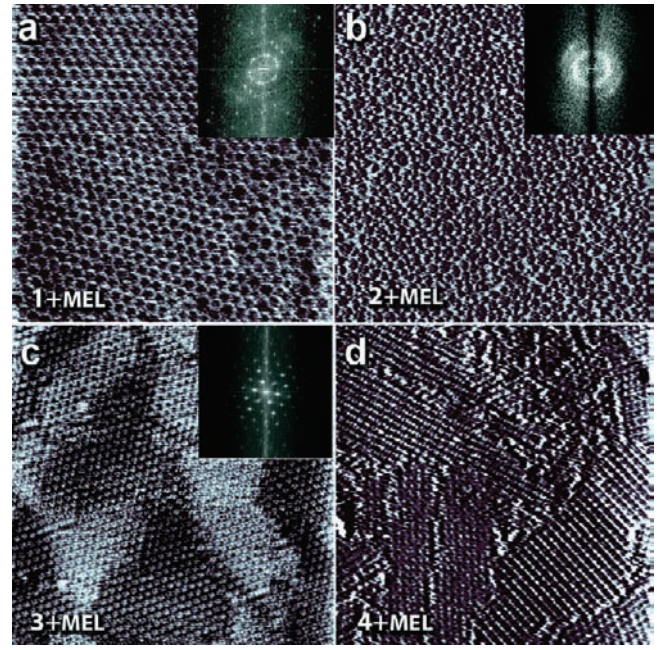

Figure 5. STM images recorded in (a), (d) constant current, and (c), (b) constant height mode featuring (i.e., 100 nm × 100 nm) the four assembling systems of linker+**MEL**. (a) **1**+**MEL** deposited from 12 μM solutions features crystalline domains at medium-length scales. Two highly ordered domains are evidenced from the Fourier transform, corresponding to the left side of the image. (b) **2**+**MEL** patterns deposited from 15 μM solution exhibiting a high polygonal dispersity. (c) **3**+**MEL** patterns from 6 μM solution of **3** and 21 μM solutions of **MEL** were found to exhibiting long-range defect-free crystalline domains. (d) **4**+**MEL** patterns from 14 μM solutions featuring multiple coexisting polymorphs. Tunneling parameters: (a) $I_t = 1$ pA, $V_t = -400$ mV; (b) $I_t = 1$ pA, $V_t = -400$ mV; (c) $I_t = 1$ pA, $V_t = -400$ mV; (d) $I_t = 20$ pA, $V_t = 500$ mV.

Polymorphism and Glasses in 2D Networks. The wide variety of hexagonal, glassy, and linear structures previously shown represents a clear example of polymorphism in 2D bicomponent networks. For the sake of comparison, the self-assembly behavior on a 100 nm × 100 nm scale of the studied bicomponent systems is shown in Figure 5 while the insets in a−c of Figure 5 report the respective 2D fast Fourier transform (FFT). It reveals that a higher degree of crystallinity is observed in system **3**+**MEL**, in particular if compared to that of **2**+**MEL**. On the other hand, system **1**+**MEL** was found to form hexagonal domains coexisting with relatively disordered areas. Time-dependent STM imaging experiments, using a fluid-cell,[78] revealed that after 12 h the degree of crystallinity of the **1**+**MEL** system in Figure 5a remains unchanged (see Figure S10). A quantitative analysis on the distribution of different polygonal structures was not possible in all binary systems since a consistent statistical estimation of the pore areas on large area STM images was beyond the limits of detection. Nevertheless, a semiquantitative description of the glass-crystal polymorphism

(78) This is accomplished with the help of a homebuilt liquid-cell, where 1 cm^2 HOPG is fitted.

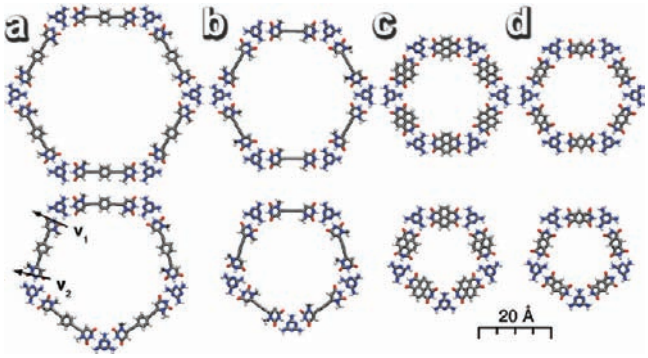

Figure 6. DFT optimized structures of isolated hexagonal (top) and pentagonal (bottom) structures with **MEL** together with (a) **1**, (b) **2**, (c) **3**, and (d) **4**.

in these 2D networks could be obtained by simulating hexagonal and other polygonal structures for each different linkers making use of DFT calculations. Figure 6 depicts the DFT optimized molecular models of hexagons and pentagons engineered combining **MEL** with linkers **1**, **2**, **3**, and **4**. The analysis of the different energetic contributions, in particular in terms of the energy needed to change the conformation of the molecular backbone and the energy of formation of hydrogen-bonds, reveals that the difference in favoring the formation of pentagons or hexagons is mostly due to the flexibility of the backbone of the linker molecules. The molecular deformation[79] energy cost, $\boldsymbol{E}_{\mathbf{def}}$, is defined as the difference between the energy of an isolated molecule in the conformation it has within a specific 2D architecture, $\boldsymbol{E}_{\mathbf{architecture}}$, and that of a relaxed isolated molecule $\boldsymbol{E}_{\mathbf{isolated}}$. Table 2 shows that $\boldsymbol{E}_{\mathbf{def}}$ remains unchanged within a few meV, for all linkers (**1**−**4**), in both hexagons and pentagons. This is because $\boldsymbol{E}_{\mathbf{def}}$ features a dominant contribution from the force needed to modify the molecular geometry in the immediate vicinity of the hydrogen-bonding moieties (i.e., from the deformation of C═O and N−H bonds, see Supporting Information Figure S13). The flexibility of the linkers' backbone is then better quantified by defining an angle β between the vectors V_1 and V_2 in the pentagon linkers in Figure 6. As expected, for pentagons with **1** and **2**, β amounts to 12.15° and 11.14°, respectively, while for pentagons with **3** and **4** β amounts to 2.90° and 2.35°. This means that the backbone flexibility of linkers **1** and **2** allows the optimal hydrogen-bond configuration, having $\beta = 12°$.

The same trend is seen for the hydrogen-bond distances (Table 2): for linkers **1** and **2** they are almost identical in hexagons and pentagons, whereas for linkers **3** and **4** there is a significant difference. $E_{\text{H-bond}}$ behaves accordingly in all cases, being less favorable for the formation of a pentagon, and more favorable for the formation of a hexagon. In the first two linkers however, the $E_{\text{H-bond}}$ difference between hexagons and pentagons is rather subtle (2 and 18 meV, respectively), whereas it increases to 68 meV for linker **3**. This further confirms that the flexibility of linkers **1** and **2** allows the system to remain in the optimal hydrogen-bond configuration in both polygons. In contrast, the lower flexibility of linker **3** affects the triple H-bond colinearity in the pentagonal structures, resulting in a less strong intramolecular interaction. Finally, the E_{def} difference between hexagons and pentagons for linker **4** is 28 meV. This suggests that if the porous network of **4**+**MEL** were observed, it would have a certain tolerance to different polygon formation, being more crystalline than **1**+**MEL** and **2**+**MEL** but less than **3**+**MEL**.

The origin of the intrinsic tightly packed polymorph of system **3**+**MEL** can be well described in analogy with similar systems studied under ultrahigh vacuum (UHV) conditions.[74] Linear assemblies of **3**+**MEL** are favored because of the additional van der Waals interactions between adjacent NTCDI cores. In fact linear assemblies are not native from **1**+**MEL** and **2**+**MEL** systems as the side chains prevent close interow interactions so only the porous patterns are predicted (Table 1). For the **3**+**MEL** system, although the *potential energy per molecule* in Table 1 predicts the formation of the hexagonal porous network phase at low equimolar concentrations, it does so by only a 0.13 eV margin (0.862 vs 0.725 eV), and as discussed, experimentally the linear **3**+**MEL** was predominantly observed. At higher **MEL** concentrations, the formation of the highly self-healed hexagonal pattern may be only stabilized through additional coadsorption of melamine. As previously discussed, Figure S9 in the Supporting Information shows a tentative coadsorbed configuration; it exhibits three coadsorbed melamines for every repeating unit, resulting in a hydrogen-bond energy gain of 0.228 eV per melamine coadsorbed. Assuming this stoichiometry to be correct, the formation of a hexagonal pattern is predicted when only five molecules are considered to form the repeating unit, three of type **3** and two of **MEL** (1.00 eV total *potential energy per molecule*, Table 1). When the actual eight molecules making up the assembly are considered, the *potential energy per molecule* of the coadsorbed hexagonal phase is lower (0.624 eV), and again the linear assembly is predicted (0.725 eV). Our observations (Scheme 2) indeed confirm that at high equimolar concentrations, unresolved areas are present alongside the coadsorbed hexagonal phase. At these high concentrations, the *potential energies per area* (Table 1) predict that pure mixtures of **MEL** (*polymorph a* 1.457 eV) and **3**+**MEL** (1.451 eV) should be formed. It is worth highlighting that linker **3** and **MEL** have previously been studied under UHV,[80] where disordered phases were observed. In turn, an expanded tetracarboxy diimide (PTCDI) exhibited[81] a very similar behavior to that of molecule **3** in the presence of coadsorbed melamine under diluted conditions (Figure 3a)[82,83] The latter evidence points out that the highly hexagonal pattern of **3**+**MEL** is in fact a local (kinetic) minimum.

As introduced in the previous section, molecular pattern **4**+**MEL** benefits not only from favorable van der Waals interactions of tightly packed structures, but also from the formation of stabilizing $[(\mathbf{4})_2(\mathbf{MEL})_2]$ tetramers. Moreover, the intrinsic hydrogen-bond formation energies of **3**+**MEL** and **4**+**MEL** dimers may further disfavor the formation of a nanoporous network over a tightly packed pattern, being 36−62 meV weaker than those for **1**+**MEL** and **2**+**MEL** assemblies.

(79) By molecular deformations we include all stretching, bending, and rotational changes of groups of atoms within a given molecule.

(80) Perdigao, L. M. A.; Fontes, G. N.; Rogers, B. L.; Oxtoby, N. S.; Goretzki, G.; Champness, N. R.; Beton, P. H. *Phys. Rev. B* **2007**, *76*, 245402–245406.

(81) Staniec, P. A.; Perdigão, L. M. A.; Saywell, A.; Champness, N. R.; Beton, P. H. *ChemPhysChem* **2007**, *8*, 2177–2181.

(82) Silly, F.; Shaw, A. Q.; Castell, M. R.; Briggs, G. A. D. *Chem. Commun.* **2008**, 1907–1909.

(83) Note however that PTCDI+Mel mixtures have been reported to form highly crystalline patterns when deposited from pure DMF and imaged at the Au(111)−air interface. Madueno, R.; Raisanen, M. T.; Silien, C.; Buck, M. *Nature* **2008**, *454*, 618–621. It is also worth noting that the PTCDI+MEL system could not be studied because of the insolubility of the PTCDI molecule in TCB, even at high concentrations of DMSO.

Table 2. Calculated $E_{H\text{-}bond}$, E_{def}, and H-Bond Distances of **MEL** with **1**, **2**, **3**, and **4**, Respectively, in Different Polygonal Structures

	linker + MEL structure	$E_{H\text{-}bond}$ [eV/H-bond]	E_{def} melamine [eV/molecule]	E_{def} linker [eV/molecule]	O−H distance [Å][a]	N−H distance [Å]
1	dimer	0.820	0.046	0.108	1.85	1.72
	isolated pentagon	0.797	0.074	0.218	1.83, 1.87	1.73
	isolated hexagon	0.799	0.075	0.224	1.85	1.73
	repeated hexagon	0.778	0.111	0.211	1.85	1.74
2	dimer	0.828	0.039	0.121	1.85	1.70
	isolated pentagon	0.784	0.078	0.255	1.83, 1.87	1.71
	isolated hexagon	0.802	0.077	0.230	1.84	1.72
	repeated hexagon	0.772	0.121	0.231	1.84	1.73
3	dimer	0.768	0.036	0.109	1.87	1.74
	isolated pentagon	0.678	0.061	0.200	1.71, 2.08	1.80
	isolated hexagon	0.742	0.075	0.229	1.82	1.72
	repeated hexagon	0.718	0.114	0.230	1.82	1.72
4	dimer	0.775	0.043	0.129	2.09	1.72
	isolated pentagon	0.716	0.082	0.232	1.89, 2.29	1.65
	isolated hexagon	0.744	0.081	0.222	2.08	1.65
	repeated hexagon	0.721	0.118	0.196	2.07	1.65

[a] For the isolated pentagons two different bond lengths for the H-bonds with oxygen acceptors have been observed.

These seemingly small differences are further increased because as patterns become more and more periodic (or crystalline), molecules surrounding melamine are subject to electrostatic repulsions, and hydrogen-bond energies are further weakened through depolarization.

The greater crystalline character of some of the **1**+**MEL** domains than those of **2**+**MEL** remains an open question. Theoretically, both systems display similar H-bond and deformation energies between hexagons and pentagons. The FFT image of Figure 5a shows two coexisting crystalline domains, rotated by 14 ± 3° relative to their unit cell vectors. Figure S11 (Supporting Information (SI)) shows that there is no preferred orientation of crystalline domains with the unit cell vectors of HOPG (which are related by 60°), pointing to a minor role played by the substrate in the crystalline nature of the patterns. Moreover, the patterns on HOPG obtained for the monocomponent system of **MEL** (see Figure S1, SI) and linker **3** (see Figure S4, SI) surprisingly correlate with architectures observed on Au(111)[32,77] and Ag/Si(111)[80,84] substrates (discrepancies in the unit cells being below 20%) confirming our hypothesis that the substrate plays a negligible role when H-bonds are involved. A possible explanation for the coexistence of glassy and crystalline phases for system **1**+**MEL** relates to the crystallization dynamics. To this end, the exact crystallization mechanism should be unraveled, albeit this is experimentally not accomplishable on the required nanoscale spatial resolution. To explore the reversible nature of the self-assembly process at the solid−liquid interface, we have performed at such interface an *in situ* thermal annealing[85] (up to 40 ± 2 °C) through a 2 h heating ramp starting at 20 ± 1 °C. Figure S7 (SI) reveals[86] that the monolayer exhibits a very limited propensity to undergo glass-crystal reorganization[87] (i.e., statistically, the polygonal distribution remained unchanged) even as the pattern appears more and more dynamic (c and d of Figure S7, SI). Likewise, the *ex situ* temperature-dependent experiments, performed by applying to the HOPG surface a 12 μM solution of linker **1** and **MEL** at different temperatures (10, 20, 30, and 40 ± 2 °C), revealed the presence of the same amount of polygons on the substrate, confirming that the crystallization process is not thermally activated in the explored temperature range. These extrinsic crystallizing conditions (temperature and concentration) do not significantly affect the polymorph distribution of the **1**+**MEL** assemblies. The lower crystallinity of the **2**+**MEL** assemblies compared to that of **1**+**MEL** could be attributed to the increased backbone flexibility of linker **2**, raising the probability of formation of larger polygons, such as heptagons and/or octagons. Temperature-dependent experiments with **2**+**MEL** phases could not be performed because the low network stability (limited to tens of minutes) during *in situ* scanning, which we tentatively ascribed to the low affinity of module **2** for HOPG.

Conclusions

In summary the comparative studies of four linkers interacting with melamine via three parallel H-bonds offered new insight on the design of preprogrammable bicomponent supramolecular 2D networks. In all the bicomponent systems, multiple phases were observed when using solution with concentration below 100 μM, confirming that a concentration-dependent polymorphism and phase segregation are hallmarks of the self-assembled structures at solid−liquid interfaces. An accurate prediction of the multiple phases encountered was achieved by purely enthalpic considerations, through DFT hydrogen-bond formation energies. Furthermore, we have proved that the polymorphism, which can also be expressed through the existence of multiple polygon structures, is an intrinsic feature of molecular design. In particular, three aspects were found to be crucial toward the formation of highly ordered and preprogrammed porous networks at the solid−liquid interface: (1) (di) acetylene fragments are not the optimal choice when looking for fully rigid molecular modules, as they introduce sufficient conformational flexibility allowing formation of polymorphic and glassy phases; (2) peripheral functionalization of the linker molecules is needed to avoid strong side-to-side interactions between the module's cores that will drive the formation of tightly packed bicomponent patterned assemblies over porous networks and, more likely, hinder the strong adsorption in the pattern's pores; (3) phase segregation and self-recognition in multicomponent systems may be avoided by preprogramming several molecular modules

(84) Keeling, D. L.; Oxtoby, N. S.; Wilson, C.; Humphry, M. J.; Champness, N. R.; Beton, P. H. *Nano Lett.* **2003**, *3*, 9–12.
(85) At higher temperatures, STM images are too noisy due to excessive thermal drift.
(86) The right border of the images in Supporting Information, Figure S7a−c, shows a coexisting phase of linker 1. This segregated phase was used as a spatial reference during the continued imaging during the heating ramp.
(87) Bigger holes in the monolayer do appear more often, as shown in Supporting Information, Figure S7c and d.

bearing complementary recognition moieties. Additionally, we have demonstrated that by unraveling the energetic contributions in crystallization, polymorphism, and phase segregation, a dramatic improvement in chemical design, and thus in the molecular engineering, can be achieved. Addressing these issues provide reliable design protocols for the precise and tunable nanopatterning of surfaces. We have also shown that the substrate plays a negligible role in the formation of networks held by trihapto hydrogen-bonding interactions, thus paving the way toward the extension of this nanopatterning protocol to a wide variety of substrates. In the limits of chemical design and crystal engineering stand biology which is able to reduce all possible intrinsic degrees of freedom into self-healing and preprogrammable self-assembly.

Experimental Section

Computational Details. All calculations were done within the framework of density functional theory (DFT) with periodic boundary conditions using the Vienna Ab-initio Simulation Package (VASP).[88] The ion-core interaction was described by the projector augmented waves method.[89,90] The generalized gradient approximation (GGA) through the Perdew−Wang 91 (PW91) functional[91] was used to describe exchange-correlation effects. The plane wave basis has been expanded up to a cutoff energy of 400 eV and only the gamma-point was used to represent the *k*-point grid. Structural optimization was done until the force acting on each atom was below 0.01 eV/Å. The **1** and **2** linker molecules were simplified by replacing the dangling alkane chains with methyl groups to reduce the computational cost. The simulated STM images were based on the Tersoff−Hamann approximation[69,70] where d*I*/d*V* is proportional to the local density of states (LDOS). The images in Figure 1b are contour plots of the densities for molecular orbitals in the energy range from the specified energy to the Fermi energy at a constant height of 3 Å above the **1**+**MEL** repeated hexagons in vacuum. As no substrate was included in the calculations, we assume that the vacuum levels of the weakly physisorbed molecules and the HOPG substrate are aligned. Energies are given relative to the Fermi energy of graphite, as obtained from the calculated work function of a single graphene sheet.

Compounds. Synthesis of molecule **1**[92] and **2**[93] are described elsewhere. Linker **3**, 1,4,5,8-naphthalenetetracarboxylic acid dyanhydride (70300, purum >95%) and melamine (**MEL**) (63600, purum >99.0%) were purchased from Fluka and used without further purification. Linker **4**, pyromellitic diimide (P1153, >95%) was obtained from TCI Chemicals Europe. 1,2,4-Trichlorobenzene (spectrophotometric grade 99%) and anhydrous DMSO (99.9%) were obtained from Alfa Aesar and Sigma-Aldrich, respectively.

STM Imaging. Mother solutions of molecules **1**, **2**, **3**, **4**, and **MEL** were prepared by dissolution of an exact weighted amount of the respective product in 500−1000 μL of DMSO. Uncertainties values are derived from the standard deviation for the "limit values" of the balance's linearity (XS105 Mettler Toledo). Intermediate solutions were then prepared to the respective concentrations with 1,2,4-trichlorobenzene (TCB). These solutions where then combined in different ratios to afford the bicomponent solutions (linker + MEL) between 1 and 100 μM (see main text for specific concentrations) used for the STM experiments. The assembly formation is typically obtained by applying 6 μL of vigorously stirred and warm (except when noted in the main text, 30−40 °C) solutions onto freshly cleaved HOPG. STM imaging was done in a commercial instrument, Veeco Multimode (Nanoscope III controller). STM tip was approached and the solution imaged before the solvent was completely evaporated (~3 h, except in the cases where a fluid cell was used, where the solvent evaporated after 2−3 days). Imaging of the patterns occurred within minutes. Unit cells were corrected by the underlying graphite. All images with superimposed molecular models were also corrected by the underlying graphite, except for linker **3** (NTCDI) in SI, where no reference could be imaged. Unit cell errors correspond to the standard deviation multiplied by a factor of 2. The models were minimized with Chem3D at the MM2 level. Unit cell determination and plane correction were made by the SPIP program. No filtering other than line-wise leveling was applied to the images herein reported, except for the images in Figure 5c and in Figure S7 (SI) where a low pass filter was applied. No high voltage (i.e., >1 V) pulses where applied at any time during image acquisition.

Acknowledgment. This work was financially supported by the European Union through the Marie-Curie Research Training Network PRAIRIES (MRTN-CT-2006-035810) and EST-SUPER (MEST-CT-2004-008128), the International Center for Frontier Research in Chemistry (FRC, Strasbourg), the Belgian National Research Foundation (FRS-FNRS, through the Contracts 2.4.625.08 and 2.4.550.09), the "Loterie Nationale", the University of Namur, and the Swedish Research Council (VR). Allocations of computer resources at the University of Liverpool and at NSC by SNAC are also gratefully acknowledged. D.B. and A.L.P. thank Prof. M. Prato for the access to the laboratory facilities in Trieste.

Supporting Information Available: This material is available free of charge via the Internet at http://pubs.acs.org.

JA9032428

(88) Kresse, G.; Furthmüller, J. *Phys. Rev. B* **1996**, *54*, 11169–11169.
(89) Blüchl, P. E. *Phys. Rev. B* **1994**, *50*, 17953–17953.
(90) Kresse, G.; Joubert, D. *Phys. Rev. B* **1999**, *59*, 1758–1758.
(91) Perdew, J. P.; Chevary, J. A.; Vosko, S. H.; Jackson, K. A.; Pederson, M. R.; Singh, D. J.; Fiolhais, C. *Phys. Rev. B* **1992**, *46*, 6671–6671.
(92) Llanes-Pallas, A.; Matena, M.; Jung, T.; Prato, M.; Stöhr, M.; Bonifazi, D. *Angew. Chem., Int. Ed.* **2008**, *120*, 7840–7844.
(93) Llanes-Pallas, A.; Bonifazi, D. Manuscript in preparation, 2009.